

Characterization of lithium-ion battery materials with SmartLab

Yuji Shiramata* and Takayuki Konya**

1. Introduction

Because lithium-ion batteries have higher energy density than other secondary batteries, it has been possible to make them smaller and lighter. This has enabled them to spread rapidly as power sources for mobile devices such as laptop computers and cellular phones. The demand for lithium-ion batteries keeps growing relentlessly and, in recent years, the electrification of vehicles using secondary batteries has become a worldwide trend toward realizing a low-carbon society. Furthermore, because conventional liquid-state cells using an organic solvent as the electrolyte are flammable, the development of safe, all-solid-state cells using a solid electrolyte is being actively pursued in Japan and the rest of the world.

In this light, many expect the performance of lithium-ion batteries to improve further, together with longer life and better safety. X-ray diffraction (XRD) is considered one of the effective analytical techniques required to evaluate the improved performance of lithium-ion batteries.

To examine the crystallization and phase ID analysis of synthesized battery materials, lab-scale X-ray diffractometers that are readily available for research are frequently used. On the other hand, *operando* (or *in-situ*) measurement of the changes in the crystal structure of the positive and negative electrode materials during the charging and discharging processes are frequently conducted at synchrotron facilities where high-intensity X-rays are available⁽¹⁾⁻⁽³⁾. Recently, *operando* measurement has become possible even with lab-scale X-ray diffractometers due to improved performance of X-ray sources, optical elements, and detectors. This article introduces examples of characterizing lithium-ion battery materials using SmartLab.

2. SmartLab X-ray diffractometer

2.1. Hardware (X-ray sources, optical systems, optical elements, and detectors)

The X-ray sources often used for analyzing battery materials are Co, Cu, Mo, and Ag. The wavelength of each X-ray source is as follows: CoK α (1.790 Å) > CuK α (1.541 Å) > MoK α (0.710 Å) > AgK α (0.560 Å). As can be seen from the equation $E = hc/\lambda$, X-rays with shorter wavelengths can penetrate the sample more due to the

high energy.

In addition to systems that use X-ray sealed tubes corresponding to each of these wavelengths, Rigaku offers systems with higher-power rotating anode X-ray tubes. When applying the output of Co (40 kV-135 mA = 5.4 kW), Cu (45 kV-200 mA = 9.0 kW), Mo (60 kV-150 mA = 9.0 kW), and Ag (60 kV-100 mA = 6.0 kW), the rotating anode X-ray tubes can produce X-rays with intensities about three to five times higher than sealed X-ray tubes. Analyzing a lithium-ion battery during rapid charging and discharging at a high current value would require time-resolved measurement to obtain XRD data at short time intervals. Even in this situation, using a high-power rotating anode X-ray tube can produce X-ray intensity high enough to analyze the battery.

Furthermore, the geometry for XRD can be switched between reflection and transmission geometry depending on the measurement purpose. The next section explains details for each geometry.

2.1.1. Reflection geometry

One reflection geometry is the Bragg–Brentano parallel focusing geometry, which uses a divergent beam. This geometry is widely used for X-ray diffractometers, from desktop models to stationary types, because it is easy to obtain high-intensity, high-resolution XRD profiles. Co, Cu, and Mo X-ray sources are often used to characterize battery materials.

Rigaku offers its original battery cell attachment, which allows observation of the crystal phase reaction in the cell during charge and discharge reactions through reflection geometry. This battery cell attachment is unique in that it uses an aluminum current collector coated with positive electrode material as the X-ray window for ease of obtaining diffraction peaks from the positive electrode material. In the past, metallic beryllium was used as the X-ray window, but that metal presented disadvantages such as (1) XRD peaks are observed from beryllium metal and beryllium oxides, substances that are hazardous to humans, and (2) the replacement cost was expensive when problems occurred with the window material. Figure 1 shows the structure of the battery cell attachment, and Fig. 2 shows the reflection geometry with the battery cell attachment mounted on the SmartLab.

In many cases, positive electrode materials are made of transition metal compounds containing manganese, iron, cobalt, nickel. Because of this, when Cu radiation is selected, fluorescent X-rays are generated from the

* Application Laboratories, Rigaku Corporation.

** Rigaku Europe SE.

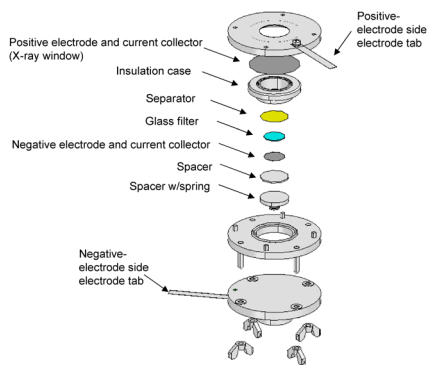


Fig. 1. Structure of the battery cell attachment.

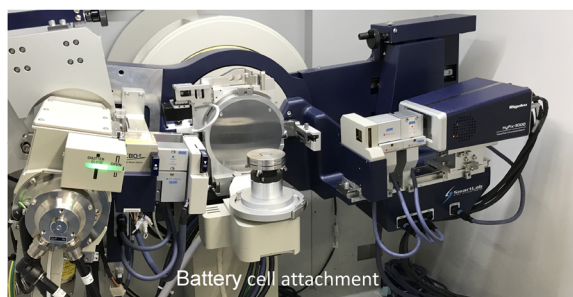


Fig. 2. SmartLab in the reflection geometry (detector is HyPix-3000).

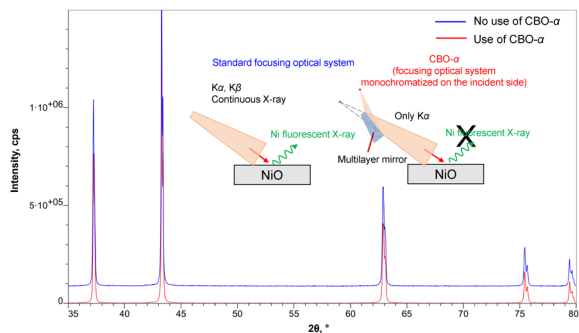


Fig. 3. XRD profile of nickel oxide (NiO) powder when using CBO- α .

sample as secondary X-rays, increasing the background level of XRD profiles. If the background level is high, the peak/background (P/B) ratio becomes smaller, increasing the error and making it harder to observe minor peaks. For this reason, background levels must be lowered.

The SmartLab has functions to obtain lower background level. One is energy discrimination functionality of D/teX Ultra250 one-dimensional semiconductor detector⁽⁴⁾ and the Hypix-3000 two-dimensional semiconductor detector⁽⁵⁾. Additionally, the SmartLab can attach flat multilayer mirrors (CBO- α)⁽⁶⁾ as incident monochromator. By employing CBO- α , which can be applied to reflection geometry using monochromatic divergent X-ray beams, it becomes possible to obtain high-resolution, low-background and high-quality XRD profiles. Figure 3

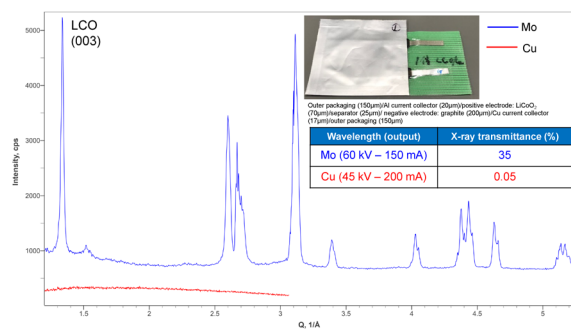


Fig. 4. Transmittance through the laminated cell when using Cu and Mo radiation and the resulting XRD profiles ($Q=4\pi \sin \theta/\lambda$ on the horizontal axis).

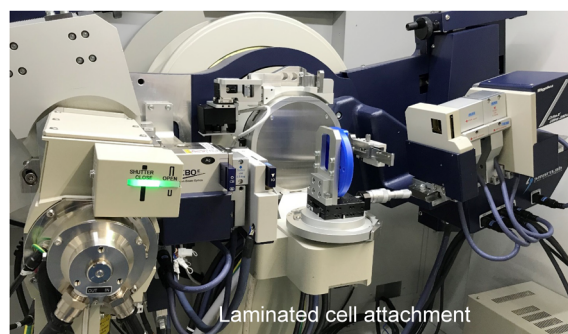


Fig. 5. SmartLab in transmission geometry (detector is D/teX Ultra250HE).

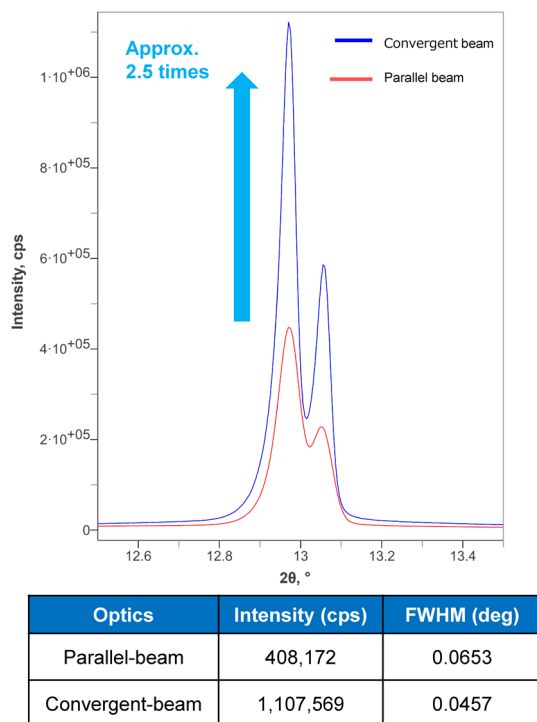


Fig. 6. Comparison of XRD profiles from the Si (111) plane between the parallel-beam optical system (CBO) and the convergent beam optical system (CBO-E) using Mo radiation.

shows the effect of CBO- α in measuring the XRD profiles of nickel oxide powder. Because the incident X-rays are monochromatized, the intensity of the X-ray fluorescence radiated from nickel is reduced due to the use of CBO- α , improving the P/B ratio dramatically.



Fig. 7. Battery evaluation system consisting of SmartLab X-ray diffractometer and HZ-7000 charging/discharging system.

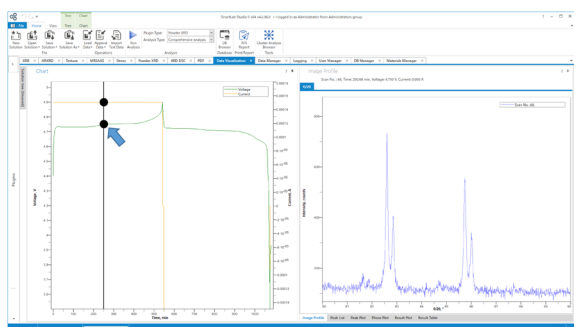


Fig. 8. An example of linking a charging/discharging profile with an XRD profile.

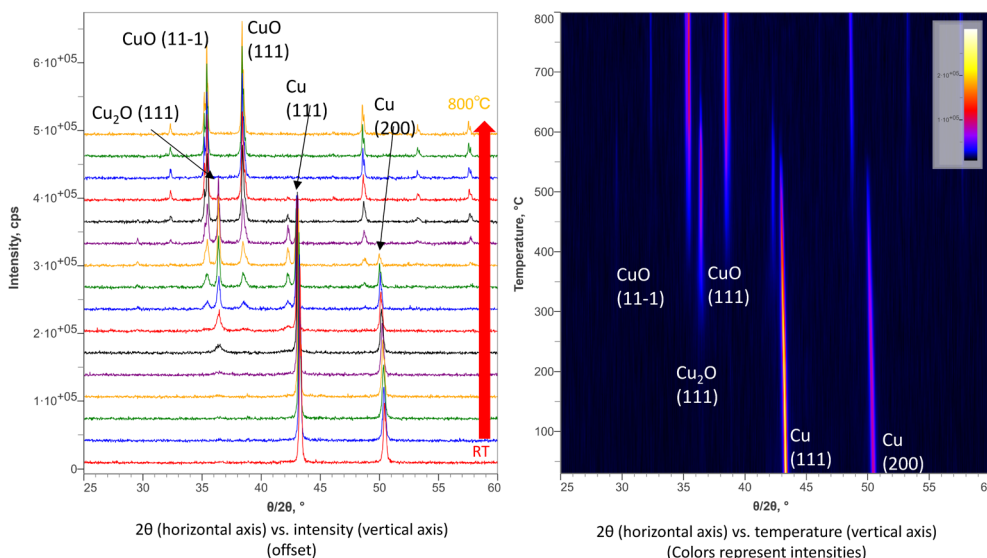


Fig. 9. Multiple XRD profiles and profile map during temperature-controlled measurements.

2.1.2. Transmission geometry

Laminated battery cells (pouch cells) are made up of laminate foil, positive electrode material, negative electrode material, a current collector, and a separator. When measuring laminated battery cell, transmission geometry is useful. In this case, both the positive and negative electrode materials can be characterized at the same time. To transmit through the sample, X-rays from Mo and Ag must be used.

Rigaku offers laminated cell attachments corresponding to various cell sizes. Figure 4 shows the transmittance and XRD profile when each X-ray transmits through the laminate cell mounted on the attachment, and Fig. 5 shows the SmartLab configuration in transmission geometry. While a sufficient amount of X-ray intensity is obtained using Mo radiation, no diffraction of X-rays from the sample is observed using Cu radiation.

In the past, transmission geometry used X-ray beams parallelized by a parabolic multilayer mirror (CBO). Under this geometry, the width of the X-ray beam would become larger on the detector, resulting in low-resolution data. For this reason, the slit width on the incident side had to be reduced, decreasing some of the X-ray intensity.

In such measurements taken using transmission geometry, the use of X-ray beams that converge on the detector with the help of an ellipsoidal multilayer mirror (CBO-E) provides high-intensity, high-resolution XRD profiles. Figure 6 shows a comparison between parallel-beam geometry and convergent beam geometry.

Furthermore, in response to the use of high-energy X-rays, Rigaku offers the D/teX Ultra250HE semiconductor detector, which has a sensor about three times as thick as the standard D/teX Ultra250, almost doubling the detector’s sensitivity.

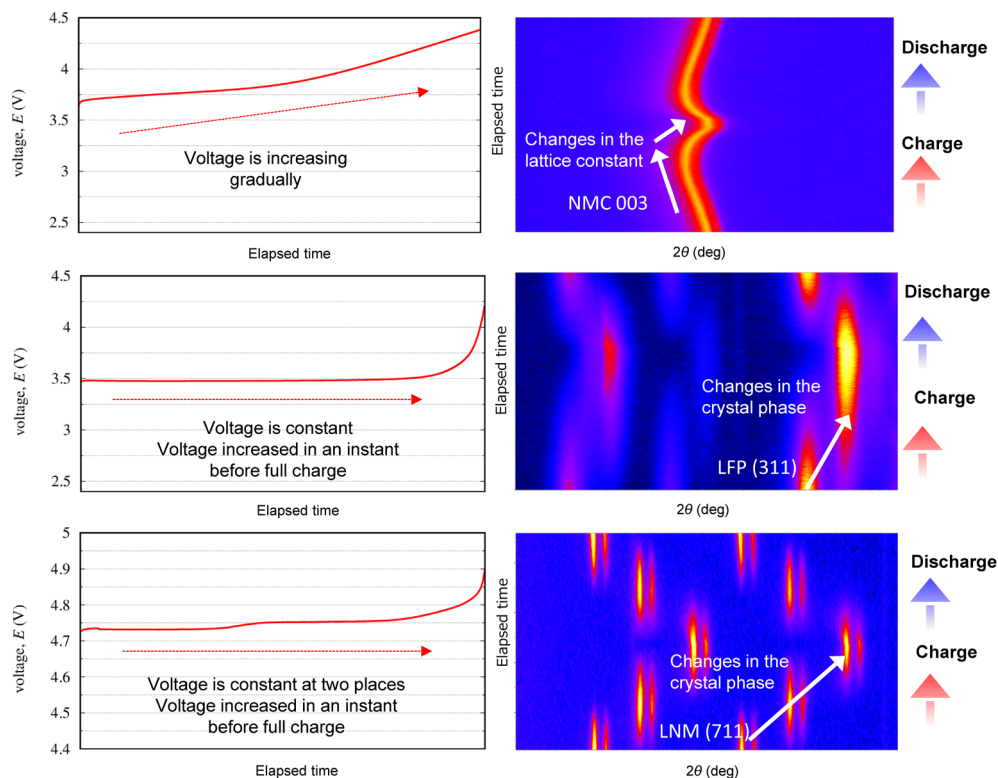


Fig. 10. Charge profiles and profile maps (using a Li half-cell as the negative electrode).

2.2. Software

SmartLab Studio II⁽⁷⁾, an integrated X-ray diffraction software package, can synchronize the charging/discharging time to the XRD measurement time by connecting to a commercially available charging/discharging device and the X-ray diffractometer via an I/O cable. Figure 7 shows a photograph of a system that combines the SmartLab and HZ-7000 (made by Hokuto Denko Corporation). It is possible to link charging/discharging profiles and XRD profiles with the help of the Data Visualization plugin in SmartLab Studio II. Figure 8 presents an example of this analysis, in which the XRD profile at the black dot in the charging/discharging profile appears.

Using the Powder XRD plugin and the Data Manager plugin makes it possible to create an offset diagram showing multiple XRD profiles, with 2θ on the horizontal axis and X-ray intensity on the vertical axis. Employing these plugins also enables the creation of profile maps in which different colors represent various X-ray intensities, with 2θ on the horizontal axis and temperature, time etc. on the vertical axis. This feature facilitates visualization of changes with time in the positions and intensity of XRD peaks. Figure 9 shows examples of an overlay display and a profile map display of XRD profiles obtained from temperature-controlled measurements. The profile map displays changing peaks in a manner that is very easy to understand.

3. Examples of XRD measurements

3.1. Using reflection geometry for *operando* measurement of various positive electrode materials in lithium-ion batteries

Laminar rock salt-type $\text{LiM}(\text{M}=\text{Ni},\text{Mn},\text{Co})\text{O}_2$, olivine-type LiFePO_4 and spinel-type LiMn_2O_4 materials are well known as positive electrode materials for lithium-ion batteries. Although each of these materials contains lithium, their conductive path for lithium ions varies depending on the crystal structure. For this reason, a good understanding of the crystal structure of each material is essential when designing lithium-ion batteries.

To observe changes in the crystal structure of each positive electrode material associated with the charging/discharging process, experimental battery cells were prepared for *operando* measurements. Each battery cell is a half-cell that contains $\text{LiPF}_6/\text{EC-DMC}$ as the electrolyte solution and metallic lithium as the negative electrode material. Figure 10 shows the charge profile and XRD profile map of each battery cell.

The details of the positive electrode materials and charging/discharging conditions were set as follows: Laminar rock salt-type $\text{Li}(\text{Ni},\text{Mn},\text{Co})_{0.33}\text{O}_2$ (NMC) [1 C = 180 mA/g, UL 4.3 V, LL 2.5 V], olivine-type LiFePO_4 (LFP) [1 C = 170 mA/g, UL 4.2 V, LL 2.0 V], and spinel-type $\text{LiNi}_{0.5}\text{Mn}_{1.5}\text{O}_2$ (LNM) [1 C = 150 mA/g, UL 4.9 V, LL 3.5 V].

The charge profile of each battery cell varied depending on the positive electrode material. The difference is related to changes in the crystal structure of the positive electrode material and the electronic state

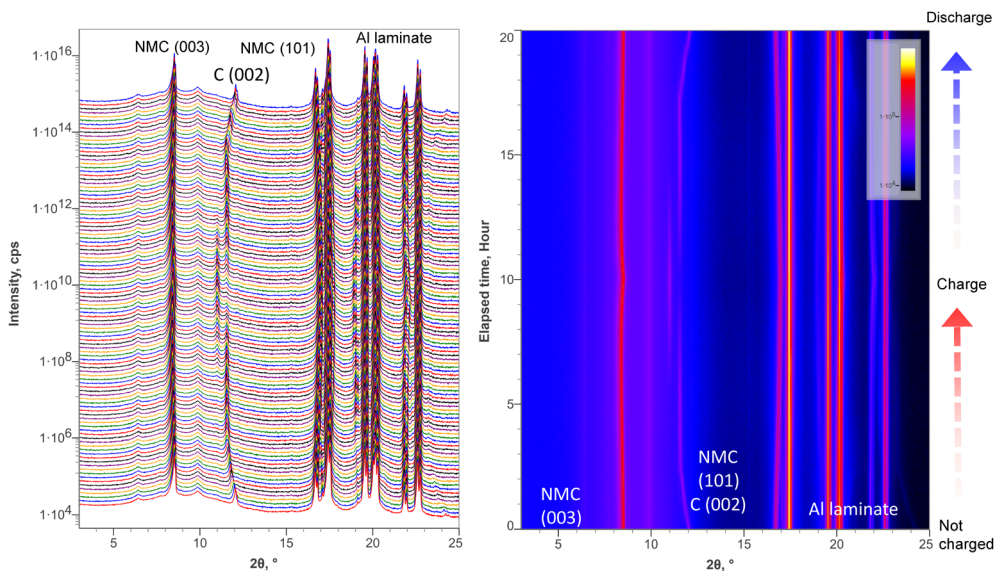


Fig. 11. Multiple XRD profiles and profile maps.

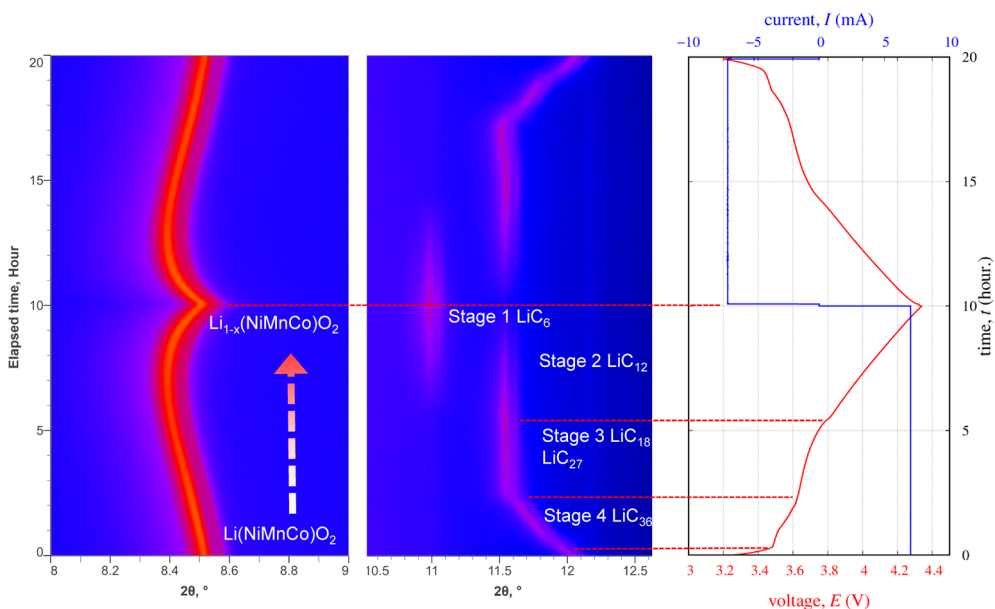
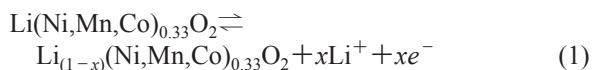


Fig. 12. Profile maps of NMC and graphite associated with a charging/discharging profile (0.1 C=7 mA).

of the transition metal ion that was oxidized or reduced.

In the case of NMC, the peak positions changed continuously. This observation suggests that a solid-solution reaction (single-phase reaction) was occurring, in which the reaction progress is driven only by the changes in the lattice constant due to lithium-ion desorption, as shown in reaction formula (1).



In the case of LFP, the peak positions did not change continuously, but a new peak appeared at a different position. This observation confirmed a transition in the crystal phase, indicating that a two-phase coexistence reaction was occurring, as shown in reaction formula (2).

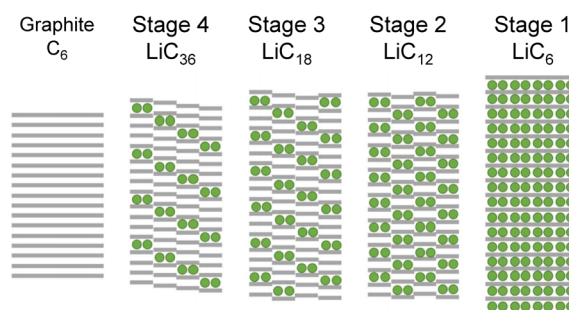
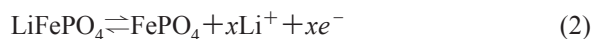


Fig. 13. Stage structures of graphite⁽¹⁰⁾.



In the case of LNM, as with LFP, observation of the changes in the peak positions revealed two two-phase

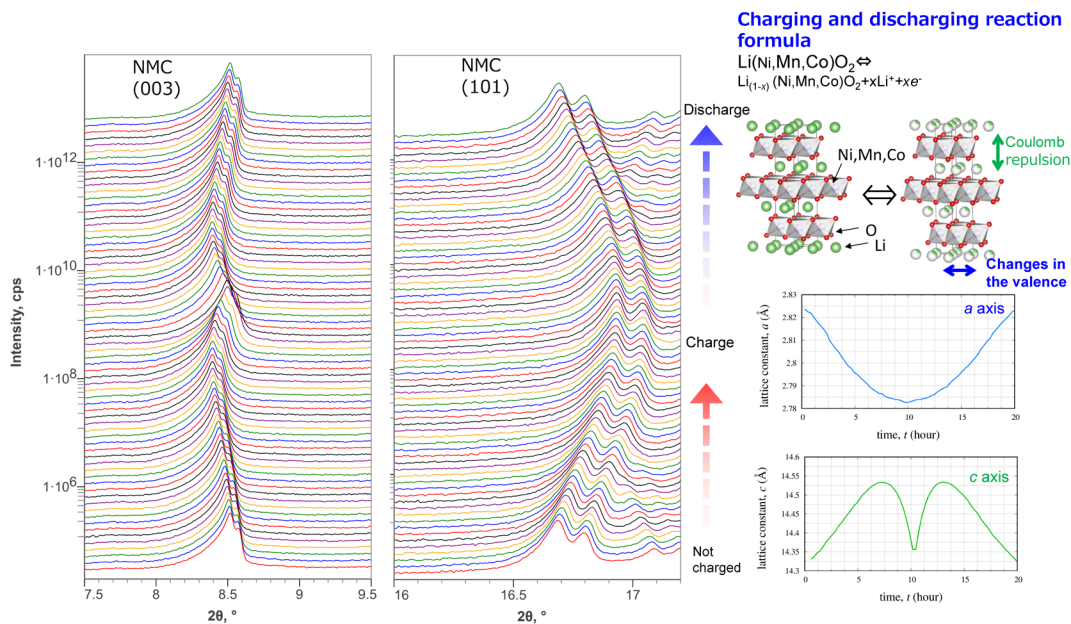


Fig. 14. Changes in lattice constant of NMC.

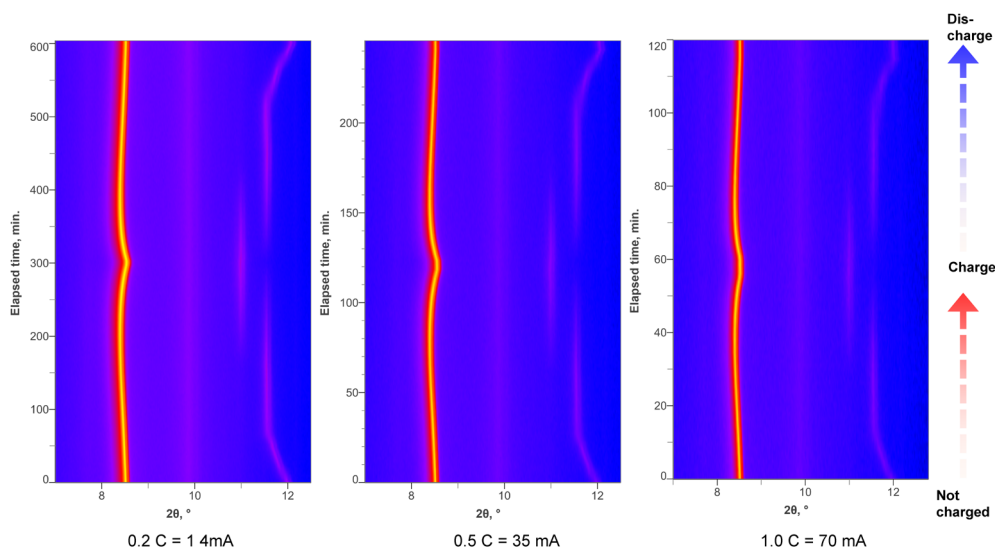


Fig. 15. Profile map at each charging/discharging rate.

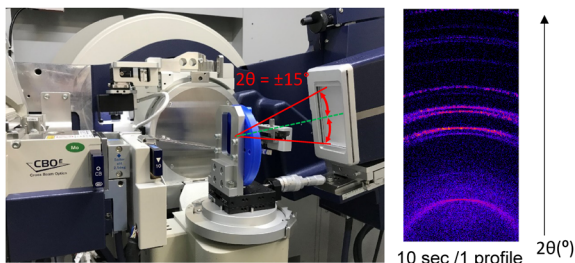
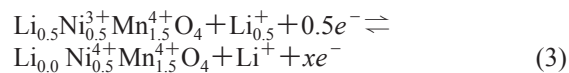


Fig. 16. HyPix-3000 in a vertical position, with two-dimensional profile.

transitions in the crystal phase, indicating that two types of two-phase coexistence reactions were occurring, as shown in reaction formula (3).



As described above, the changes in the charge/discharge profile and positive electrode material are related to each other. Therefore, the changes in the crystal structure occurring during charging/discharging can be revealed⁽⁸⁾ by analyzing the XRD profiles obtained from *operando* measurements.

3.2. *Operando* measurement of positive electrode material $\text{Li}(\text{Ni}_{0.5}\text{Mn}_{0.3}\text{Co}_{0.2})\text{O}_2$ and negative electrode material graphite in a lithium-ion battery using transmission geometry

Transmission measurement of a laminated cell using Mo or Ag radiation has the advantage of being able to measure the positive and negative electrode materials

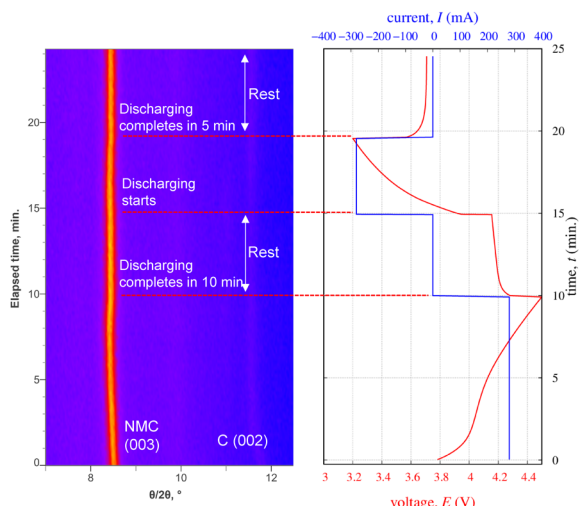


Fig. 17. Profile map and charging/discharging profile (4.0C=280mA).

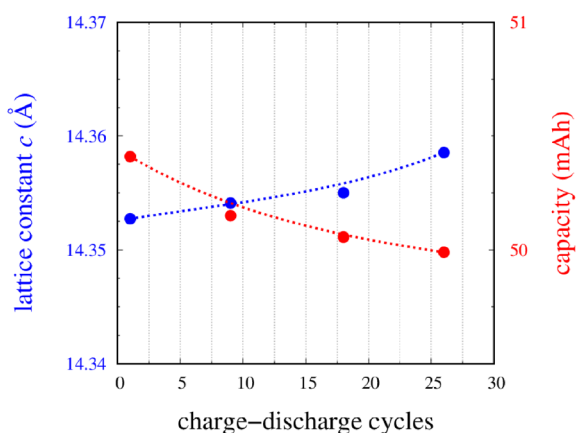


Fig. 18. Changes in the lattice constant c and the capacity of NMC during charging/discharging cycles.

simultaneously in conditions similar to the form of a battery product. A laminated full cell containing positive electrode material NMC with an atomic ratio of Ni:Mn:Co=5:3:2 and negative electrode material graphite were characterized in several ways, examples of which are shown below. The components in the laminated cell and their thicknesses are as follows: Outer packaging (100 μ m); Al current collector (15 μ m); positive electrode material-NMC (70 μ m); separator (25 μ m); negative electrode material-graphite (100 μ m); Cu current collector (10 μ m); outer packaging (100 μ m). The electrolyte solution is LiPF₆/EC-DMC.

3.2.1. Characterizing the changes in the crystal structure during the charging and discharging process

Figures 11 and 12 show the results of charging/discharging profiles and XRD profile measurements when setting the conditions at 0.1C=7mA, UL 4.3V, LL 3.2V. The results confirmed changes in the lattice constant associated with lithium-ion desorption from the positive electrode material, as well as changes in the stage structures of the negative electrode material

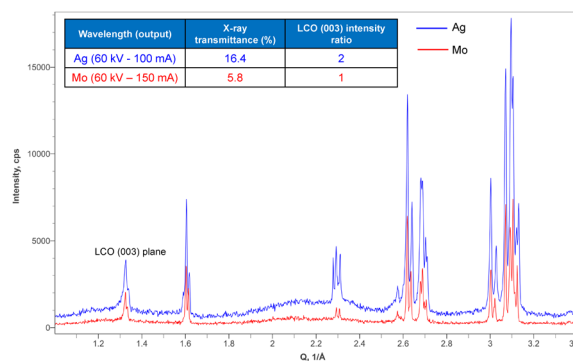


Fig. 19. The transmittance through all-solid-state batteries and the resulting XRD profiles when using Mo and Ag radiation (Q on the horizontal axis).

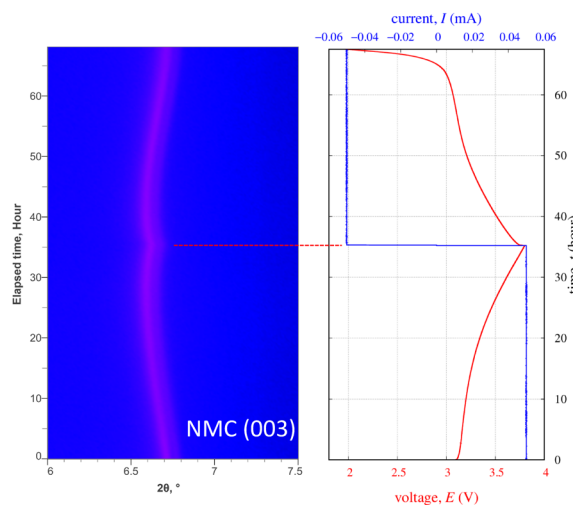


Fig. 20. Profile map and charging/discharging profile of an all-solid-state battery (0.05C=84mA/g).

graphite⁽⁹⁾. Figure 13 shows stage structure models⁽¹⁰⁾.

Figure 14 presents the plotted lattice constants a (Å) and c (Å) of the trigonal system NMC that were calculated from the (101) and (003) planes, respectively. As a result of charging, the valence of the transition metal ion changed, shrinking the a -axis. On the other hand, the c -axis expanded because the Coulomb repulsion between oxide ions increased due to lithium-ion desorption. However, the c -axis contracted an instant before full charge. There are reports attributing this contraction of the c -axis to the phenomenon that when lithium ions desorb at a specific threshold value or above, the covalent bonding between transition metal ions and oxide ions increases, and the Coulomb repulsion between oxide ions themselves decreases⁽¹¹⁾.

3.2.2. Characterizing stability at each charging/discharging rate

As shown in the results of measurements at 0.2C=14mA, 0.5C=35mA, and 1.0C=70mA, both the positive and negative electrode materials showed reversible reactions, indicating that the battery cell was operating stably at each charging/discharging rate. Figure 15 shows the obtained profile maps.

Next, the battery cell was measured at a fast-charging/d

discharging rate of $4C=280\text{ mA}$. This high charging/discharging rate means that the XRD profiles have to be measured expeditiously. For this reason, the battery cell was measured at intervals of 10 s using the HyPix-3000 two-dimensional semiconductor detector. By setting the HyPix-3000 in a vertical position, the battery cell could be measured within the range of $2\theta=\pm 15^\circ$ from the center of the detector in one measurement. This made it possible to observe fully and expeditiously the angle range needed for this analysis (Fig. 16).

Figure 17 shows the actual measurement of the battery cell at a high charging/discharging rate. At $4C$, little change was observed in the peak position of the NMC (003) plane. As a result, the theoretical battery capacity was not available. As this example shows, observing the change in crystal phase for each charging/discharging rate is considered useful for battery design and performance verification.

3.2.3. Observing changes in the lattice constant associated with capacity degradation

The capacity of a battery cell will degrade as the number of charging and discharging cycles increases. Many factors are responsible for this phenomenon, but especially in a lithium-ion battery using graphite as the negative electrode material, side reactions are actively occurring on the negative electrode surface that involve reduction and decomposition. These side reactions will consume the lithium ions supplied from the positive electrode, reducing the total number of movable lithium ions as the number of cycles increases. Consequently, the theoretical battery capacity will deteriorate. This battery cell performed 35 charging/discharging cycles at $1C=70\text{ mA}$. The lattice constant c (\AA) calculated from the NMC (003) plane after each cycle and the capacity (mAh) were measured, the results of which are plotted in Fig. 18. As the capacity of this battery cell degrades, not all the lithium ions will return to the positive electrode material, causing the lattice constant to expand with time. Observing the changes in the lattice constant is a simplified way to characterize the degradation of a battery cell's capacity with time.

3.3. Operando measurement of positive electrode material $\text{Li}(\text{Ni},\text{Mn},\text{Co})_{0.33}\text{O}_2$ (NMC) in an all-solid-state lithium-ion battery using transmission geometry

All-solid-state batteries use solid sulfide and oxide as the electrolyte, with heavy metal employed as the current collector in some cases. For this reason, the transmittance of X-rays through this battery is inevitably low. The transmittance and XRD profile of an all-solid-state battery whose laminated cell contained the following components (thicknesses) were measured using Mo and Ag radiation: Outer packaging ($150\text{ }\mu\text{m}$); Au current collector (40 nm); positive electrode material-NMC- Li_3PS_4 composite ($75\text{ }\mu\text{m}$); solid electrolyte: Li_3PS_4 ($600\text{ }\mu\text{m}$); negative electrode material-Li-In ($100\text{ }\mu\text{m}$); Cu current collector ($10\text{ }\mu\text{m}$); outer packaging ($150\text{ }\mu\text{m}$). As shown in Fig. 19, Ag

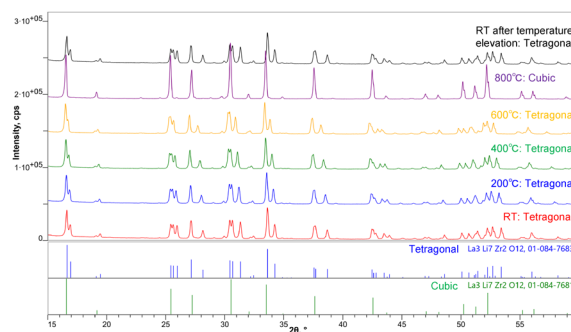


Fig. 21. Multiple XRD profiles of LLZ at each temperature.

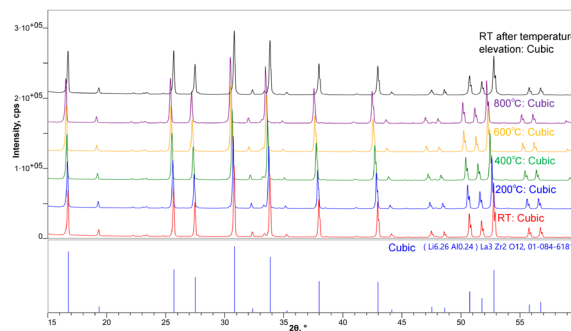


Fig. 22. Multiple XRD profiles of LALZ at each temperature.

radiation with a shorter wavelength resulted in an XRD profile with a higher intensity. The use of Ag radiation can produce higher-intensity XRD profiles depending on the types of components used in a battery cell.

The XRD profile of this battery cell was measured using Ag radiation at a charging/discharging condition of $0.05C=85\text{ mA/g}$, UL 3.8 V, LL 1.9 V. The results indicated that the change in the peak position of the NMC (003) plane could be measured well, as shown in Fig. 20.

3.4. Characterizing the crystalline system of solid electrolyte $\text{Li}_7\text{La}_3\text{Zr}_2\text{O}_{12}$

$\text{Li}_7\text{La}_3\text{Zr}_2\text{O}_{12}$ (LLZ), which is a type of oxide solid electrolyte, shows high lithium-ion conductivity at room temperature and is stable against metallic lithium. For this reason, many expect that this material will enter practical use in the future. However, its lithium-ion conductivity varies depending on the crystal system. Specifically, cubic LLZ shows a high ion conductivity of 10^{-3} S cm^{-1} , while tetragonal LLZ shows a low ion conductivity of 10^{-6} S cm^{-1} or less. For this reason, the crystal system of LLZ must be controlled to maximize its performance as an electrolyte. There are reports suggesting that the crystal system of LLZ can remain cubic even at room temperature by the solid solution of a metallic ion such as Al⁽¹²⁾.

To characterize the effect of solid-dissolved ions on the crystal system, simple LLZ and $\text{Li}_{7-x}\text{Al}_x\text{La}_3\text{Zr}_2\text{O}_{12}$ (LALZ), which is LLZ with Al in solid solution, were heated to 900°C using a high-temperature sample

chamber. Figures 21 and 22 show the results of *in-situ* measurements in a nitrogen atmosphere at intervals of 100 to 200°C in the temperature range of room temperature to 900°C.

The results showed that simple LLZ changed from tetragonal to cubic between 600 and 700°C, and returned to tetragonal after cooling back down to room temperature.

On the other hand, as reported, LALZ maintained a tetragonal system in all temperature ranges.

4. Summary

Structural studies on the positive electrode materials, negative electrode materials, and solid electrolytes used in lithium-ion batteries are essential for improving battery performance. In this respect, the importance of X-ray diffraction analysis is critical.

To realize *operando* measurements, SmartLab features reflection-type optical systems for battery cells as well as transmission-type optical systems for laminated battery cells. At the same time, SmartLab is capable of data measurement and analysis by synchronizing the battery charging/discharging process with the XRD data collection process. It is our hope that the battery characterization system SmartLab provides will contribute to the evolution of batteries in the future.

Acknowledgment

We are most grateful to Prof. Tatsuya Nakamura of the Graduate School of Engineering, University of Hyogo, Tatsumisago and Hayashi Laboratory at the Graduate School of Engineering, Osaka Prefecture University, and Mr. Hironobu Tsuji of Toray Research Center, Inc. for providing samples and advice on measurements.

References

- (1) J. B. Leriche, S. Hamlet, J. Shu, M. Morcrette, C. Masquelier, G. Ouvrard, M. Zerrouki, P. Soudan, S. Belin, E. Elkaim and F. Baudalet: *J. Electrochem. Soc.*, **157** (2010), A606–610.
- (2) W. S. Yoon, K. W. Nam, D. Jang, K. Y. Chung, J. Hanson, J. M. Chen and X. Q. Yang: *J. Power Sources*, **217** (2012), 128–134.
- (3) Y. H. Cho, D. Jang, J. Yoon, H. Kim, T. K. Ahn, K. W. Nam, Y. E. Sung, W. S. Kim, Y. S. Lee, X. Q. Yang and W. S. Yoon: *J. Alloys and Compounds*, **562** (2013), 219–223.
- (4) *Rigaku Journal (English version)*, **30** (2014), No. 1, 35–38.
- (5) *Rigaku Journal (English version)*, **30** (2014), No. 2, 38–40.
- (6) T. Osakabe: *Rigaku Journal (English version)*, **33** (2017), No.1, 15–19.
- (7) *Rigaku Journal (English version)*, **33** (2017), No.2, 29–31.
- (8) T. Konya, Y. Shiramata and T. Nakamura: *Powder Diffraction*, **34** (2019), S8–S13, doi:10.1017/S0885715619000083.
- (9) T. Ohzuku, Y. Iwakoshi and K. Sawai: *J. Electrochem. Soc.*, **140** (1993), 2490–2498.
- (10) D. Allart, M. Montaru and H. Gualous: *J. Electrochem. Soc.*, **165** (2018), A380–387.
- (11) K. Ishidzu, Y. Oka and T. Nakamura: *Solid State Ionics*, **288** (2016), 176–179.
- (12) M. Matsui, K. Sakamoto, K. Takahashi, A. Hirano, Y. Takeda, O. Yamamoto and N. Imanishi: *Solid State Ionics*, **262** (2014), 155–159.